Hindawi
International Journal of Antennas and Propagation
Volume 2019, Article ID 3137583, 10 pages
https://doi.org/10.1155/2019/3137583

Research Article

Channel Characteristics of High-Speed Railway Station Based on Ray-Tracing Simulation at 5G mmWave Band

Lei Xiong,[1] **Haiyang Miao**,[1] **Bo Ai**,[1] **Tutun Juhana**,[2] **and Adit Kurniawan**[2]

[1]*The State Key Laboratory of Rail Traffic Control and Safety, Beijing Jiaotong University, 100044 Beijing, China*
[2]*School of Electrical Engineering and Informatics, Institut Teknologi Bandung, Jl. Ganesa No. 10, Bandung, Indonesia*

Correspondence should be addressed to Lei Xiong; lxiong@bjtu.edu.cn

Received 3 May 2019; Accepted 15 July 2019; Published 2 September 2019

Guest Editor: Marko Sonkki

In order to satisfy the increasing demand for the higher transmission capacity of "smart station", millimeter wave (mmWave) technology is expected to play a significant role in the high data rate communication system. Based on the ray-tracing simulation technology, this paper would study wireless channel characteristics of the three-dimensional (3D) model of high-speed railway station at the mmWave band. Key parameters such as path loss exponent, shadow fading factor, delay spread, Rician *K*-factor, angular spread, power angle spectrum, and spatial correlation are extracted and investigated. These channel characteristics are of value for the selection of antenna arrays and even the design of future 5G communication networks in the railway environment.

1. Introduction

Nowadays, with the convenience and flexibility of high-speed railway (HSR), more and more people prefer to take rail traffic for travel or for work. In order to meet these goals in regard to safety, convenience, and efficiency, the investigations about the fifth-generation (5G) wireless communication system have become a trend [1–4] in different railway scenes. At present, the first 5G smart railway station has been established at Shanghai Hongqiao Railway Station, which is expected to have the ability to guarantee the 5G network depth coverage in this year. Smart railway station would show the wisdom of railway technology to the public from the perspective of operation and service, including indoor navigation, face identification, and 5G-guided robot. In other words, smart station has been the vital application environment in intelligent transportation systems (ITSs) [5, 6] and the analysis of the wireless channel model in the railway system for the 5G communication system is essential.

To meet the demand for seamless high data rate wireless connectivity for railway services, the efficient transmission technologies like massive multiple-input multiple-output (MIMO) is proposed [7] to improve system capacity and data rate. The large-scale fading characteristics of different railway scenarios have been summarized for the first time in [8]. Based on [8], it is noted that railway station [9, 10] is significantly different from common public network scenarios or other high-speed railway scenarios (such as viaducts, cuttings, tunnels, etc.) [11]. In [11], the authors also explored channel characteristics in different HSR scenarios by the 3D ray tracing (RT) [12–14] which could compensate for the shortcoming of traditional models and accurately analyze the special channel characteristics in 5G systems. Previous simulations focused on the single-input single-output (SISO) system and MIMO channel for indoor and outdoor communication [15–17], but they missed the research of multipath parameters such as spatial correlation in the railway system. As a result, there is still an urgent demand for a complete investigation by considering large-scale parameters, small-scale parameters, and spatial parameters [18, 19] for station scenario in MIMO systems.

This paper mainly focuses on the medium HSR station, which is the most common station scenario with two platforms and four lines. First of all, channel parameters such as path loss exponent, shadow fading factor, multipath delay, and angular spread can be obtained based on RT. The experiment will be carried out at the HSR station where base

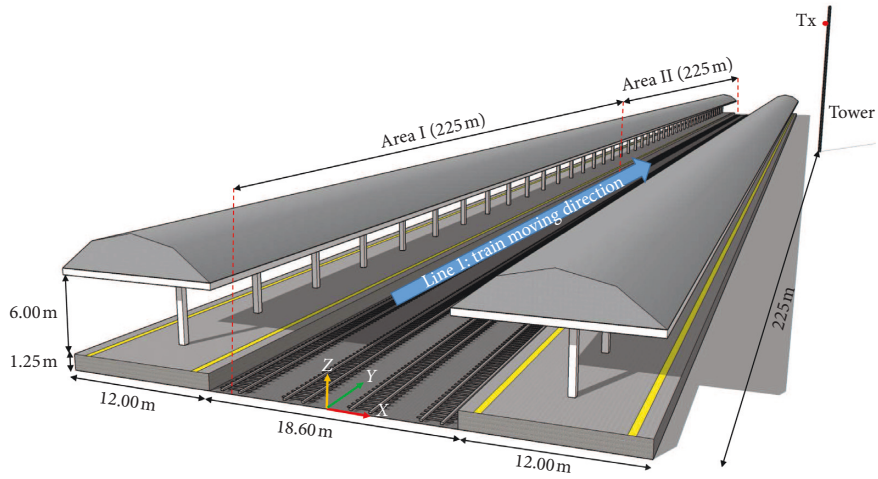

Figure 1: High-speed railway station scenario. Line 1 is divided into two parts: Area I (the area of Rx approaching the Tx) and Area II (the area of Rx leaving the Tx).

station antennas are arranged on the tower. On the contrary, the strengths of the massive MIMO system to compensate for the high path loss of the mmWave band have made high carrier frequencies become an integral component of the upcoming 5G networks. Because of the available larger transmission bandwidths, the 5G network is able to supply high data rates and enhance the quality of experience. Although propagation signals at higher frequencies have the higher path loss and are more susceptible to rapid signal degradations caused by moving or fixed obstacles [20], higher frequencies can allow the deployment of smaller antennas which enables the function of multiantenna technology to be integrated into the antenna array. In this paper, not only have the channel characteristics that can guide 3D channel modeling in 5G environment been discussed but optimized deployment recommendations have also been provided for antenna configuration based on the spatial correlation in massive MIMO systems at 37.0–42.5 GHz mmWave band.

The rest of the paper is organized as follows. The defined high-speed railway station scenario and simulation parameters are presented in Section 2. The wireless channel model for the station scenario is provided in Section 3. According to simulation results, we point out the main channel characteristics to discuss the antenna deployment in Section 4. Conclusions are drawn in Section 5.

2. Ray-Tracing Simulation

2.1. Scenario Modeling. As shown in Figure 1, the 3D scenario model with a 450 m (length) high-speed railway station is established by SketchUp in the three-dimensional Cartesian coordinate system. There are 6 types of objects and 6 materials (Table 1) in the scenario model. The LOS paths, scattering, and up to 2nd-order reflections are considered, and the initialized dielectric parameters are listed in Table 2.

Then, referring to the CRH380A, the high-speed train model is built in Figure 2. With simulation and measurement results, the effect of adjacent train compartments almost can be ignored for the received signal, which indicates the front of the train could be considered individually in the simulation environment.

Table 1: Scenario composition.

Object	Material
Platform	Granite, brick, plaster
Canopy	Plaster, metal
Ground	Tiles-rough
Rail	Metal
Crosstie	Concrete
Single-tube tower	Metal

Table 2: Material parameters.

Material	Relative permittivity	Loss tangent
Granite	4.91	0.14
Brick	4.20	0.39
Plaster	2.50	2×10^{-3}
Metal	1.00	10^{7}
Tiles-rough	3.77	3×10^{-3}
Concrete	5.60	0.05

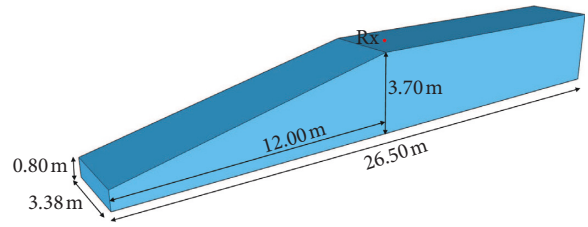

Figure 2: High-speed train model (CRH380A).

2.2. Ray-Tracing Simulation Parameters. In Figure 1, the height of the single-tube tower next to the high-speed railway station is 40 m [21]. The distance from the center line of the tower to the edge of station platform is 10 m, and the

distance to the X-axis is 225 m. The omnidirectional vertical polarization antenna is employed in this work. As the transmitter (Tx) antenna, the base station antenna is deployed on a platform of tower [21] whose height is 38.5 m and vertical distance to the center line of the tower is 0.8 m. Hence, the coordinates can be set to (30.5, 225, 38.5).

In the top view of Figure 1, simulating on Line 1, the process of passing the train through the station on Line 1 is divided into Area I where the train is approaching the tower and Area II where the train is leaving the tower. The top antenna is the receiver (Rx) which is located at the middle line on the top of train, and the vertical distance to the rear section of the train is 13 m. The Rx antenna moves along the positive direction of Y-axis, and the height is 4.16 m which is the sum of the distance to the top of train (0.15 m), the height of the train (3.70 m), and the height from the bottom of the train to the ground (0.31 m). The Y-axis coordinate of Rx antenna is 0 : 2:450 on Line 1. The key configurations of ray-tracing simulation are listed in Table 3.

Table 3: Simulation parameters.

Parameter	Value
Frequency (GHz)	37.0–42.5
Bandwidth (GHz)	5.5
Resolution (MHz)	5.5
Reflection order	2
Scattering mode	Directive mode
Antenna (Tx, Rx)	Omnidirectional vertical polarization
Tx antenna gain (dBi)	10
Rx antenna gain (dBi)	3
Tx height (m)	38.5
Rx height (m)	4.16
Tx transmit power (dBm)	43
Tx coordinate	(30.5, 225, 38.5)
Rx coordinate	(−7.5, y, 4.16)

3. Wireless Channel Model

In signal processing and wireless communication, the channel transfer function $H(f)$ at frequency f is expressed as the coherent sum of different multipath components $H_n(f)$ coupling with the polarimetric Tx and Rx antenna radiation patterns $(G_{\mathrm{Tx}}, G_{\mathrm{Rx}})$ [22].

$$H(f) = \sum_{n=1}^{N} G'_{\mathrm{Tx}} H_n(f) G_{\mathrm{Rx}},$$
$$H_n(f) = a_n(f) e^{j\Psi_n(f)} \delta\left(\phi_{\mathrm{AoD}} - \phi_{\mathrm{AoD},n}\right)\delta\left(\theta_{\mathrm{AoD}} - \theta_{\mathrm{AoD},n}\right) \cdot \delta\left(\phi_{\mathrm{AoA}} - \phi_{\mathrm{AoA},n}\right)\delta\left(\theta_{\mathrm{AoA}} - \theta_{\mathrm{AoA},n}\right), \quad (1)$$

where N denotes the number of multipath, a_n and Ψ_n are the signal amplitude and phase, respectively, ϕ_{AoD}, ϕ_{AoA}, θ_{AoD}, and θ_{AoA} are the azimuth angle of departure/arrival and elevation angle of departure/arrival, respectively [23], all of which are for the n-th multipath component.

In addition, in the wireless channel model, the line-of-sight (LOS) paths and the non-line-of-sight (NLOS) paths are usually separated because the LOS paths are obvious, whereas the NLOS paths are based on the simulation transmission modes of the RT platform including reflection, scattering, and diffraction.

4. Wireless Channel Characteristics

In this section, the simulation results of high-speed railway station on Line 1 are presented and analyzed. Furthermore, suggestions on optimized antenna array deployment are also provided.

4.1. Path Loss and Shadow Fading. Path loss refers to the loss caused by the diffusion of electromagnetic wave energy when the wave propagates. From the macroscopic point of view, it is reflected in the function of the received signal power changing with distance.

By analyzing the channel data obtained by the RT simulation platform, with the change of Y-axis coordinate of the Rx antenna, the path loss is shown in Figure 3.

In Figure 3, the path loss is almost symmetrical with respect to the Y-axis coordinate of Tx, whose maximum is 132.2 dB when the Y-axis coordinate is 22 m. In [24], assuming that the receiving sensitivity of the Rx antenna is −125.23 dBm and combining the parameters of Table 3, the maximum allowable of path loss is about 148.73 dB considering penetration loss.

In this paper, the fitting results of path loss, by the model in (2) that combines the path loss and shadow fading [25], are shown in Figure 4:

$$\mathrm{PL}(d) = A + 10n\log_{10}(d) + X_\sigma, \quad (2)$$

where A is the interception, d is the distance between the Tx antenna and the Rx antenna (unit: m), and n is the path loss exponent. X_σ indicates the zero mean Gaussian random variable with a standard deviation σ which is the shadow fading factor reflecting the large-scale fading that is caused by obstacle occlusion on the wireless channel.

From Section 2, Line 1 is divided into Area I and Area II. The fitted parameter values are shown in Table 4.

According to Figure 4 and Table 4, on Line 1, as a result of a few obstacles (such as canopy) in the scenario, the fitting path loss exponent ($n = 2.26$) is slightly larger than that in the free space path loss (FSPL) model ($n = 2$). In Area I, n is 2.69 because of more obstacles. It should be noted that n is 1.83 in Area II on account of the superposition of the LOS path, more reflection, and scattering which can be found in [11] regarding rich multipath propagation at mmWave channels. In addition, all shadow fading factors σ in the scenario are close to 6 dB which is the value of the LOS environment for rural macro (RMa) scenario in 3GPP [26].

4.2. RMS Delay Spread. Figure 5 shows the mean root mean square (RMS) delay spreads and cumulative distribution functions (CDFs) of RMS delay spreads.

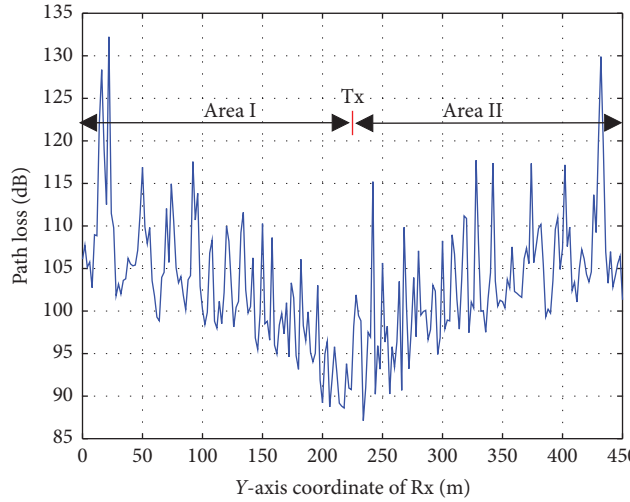

Figure 3: Path loss.

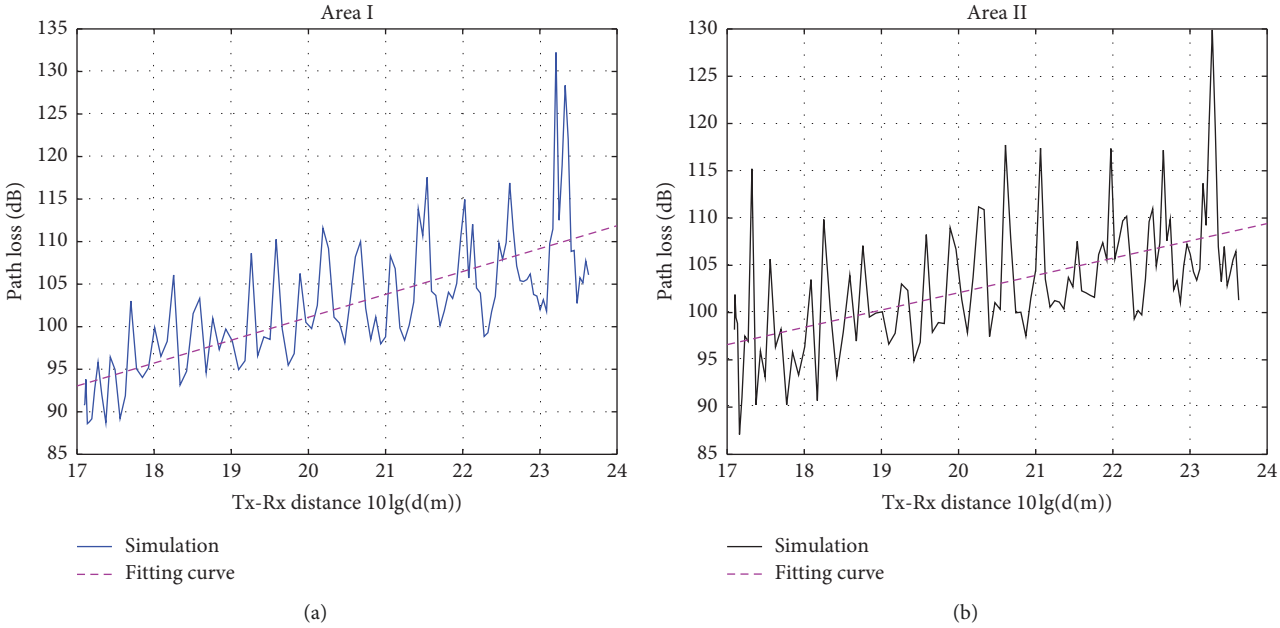

Figure 4: Simulation and fitting results. (a) Area I. (b) Area II.

Table 4: Parameter fitted value.

Parameter	A	n	σ (dB)
Area I	47.31	2.69	5.52
Area II	65.52	1.83	5.69
Line 1	56.42	2.26	5.66
FSPL	64.27	2.00	—

In Figure 5(a), the RMS delay spread curve is almost symmetric. The RMS delay spreads near Tx antenna are larger than the two ends of the station. The mean RMS delay spread 0.28 ns on Line 1 is less than the measurement result of delay spread 0.8 ns in rural [4] because the semiclosed station space limits the range of multipaths [11]. Simultaneously, due to the high-speed railway station is a semilimited type, the rays are occluded and reflected by various buildings and the train body during the propagation process. LOS paths provide the primary energy, and the RMS delay spreads are relatively small. In Figure 5(b), all values of RMS delay spread on Line 1 are less than 1.2 ns, which mean most of the powerful multipath components are concentrated around LOS path in the time delay domain. The mean values of RMS delay spread are shown in Table 5, and values of two areas are almost the same which

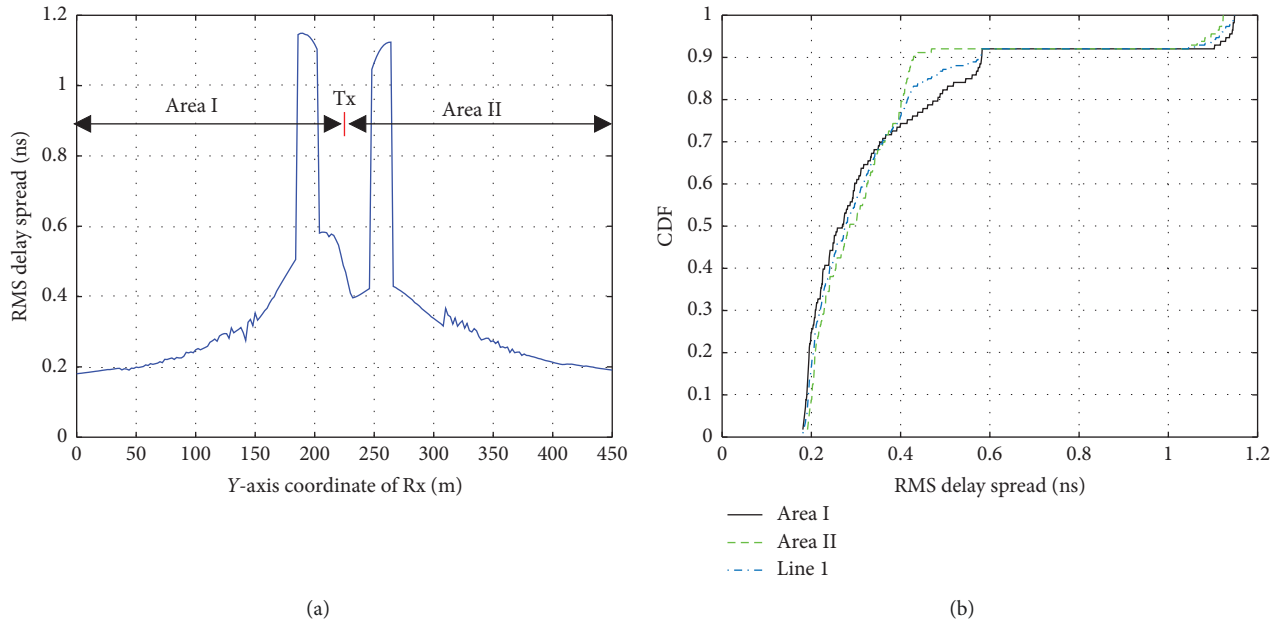

Figure 5: (a) RMS delay spread. (b) CDF of RMS delay spread.

Table 5: Mean value of parameters.

Parameter	Area I	Area II	Line 1
RMS delay spread (ns)	0.27	0.29	0.28
K (dB)	28.97	27.47	28.72

suggest Line 1 has the similar channel characteristics in the time delay domain.

4.3. Rician K-Factor. From the analysis of previous chapters, there are LOS paths and a large number of NLOS paths on Line 1. So it is indispensable to analyze the relationship between LOS path and NLOS path with the Rician K-factor [27].

With the Y-axis coordinate position of Rx antenna changing, the Rician K-factor is shown in Figure 6(a). Additionally, Figures 6(b)–6(d) demonstrate CDFs and fitting results of Rician K-factor. The mean values of the Rician K-factor are summarized in Table 5.

As shown in Figure 6(a), with the Rx antenna close to Tx antenna (Area I), the overall process of Rician K-factor is a decreasing trend. Rician K-factors near Tx antenna are the smallest, whose fluctuation is relatively serious. Conversely, in Area I and Area II, the Rician K-factors become larger with the distance between Tx antenna and Rx antenna increasing, which denotes the fading is getting weaker.

In Table 5, the mean of Rician K-factor on Line 1 is 28.72 dB that is far greater than 0 dB, which means LOS path contributed the main energy. The similar observation at mmWave band could be found in rural scenario [4] regarding the mean value 25.7 dB. As shown in Figures 6(b)–6(d), it should also be noted from the fitting results that Rician K-factors obey the Gaussian distribution owing to the wideband channel characteristic of the 5G communication system. Furthermore, when the bandwidth is wider, the multipath resolution capability that leads to a decrease in the power of the NLOS component of the main path gets stronger, so Rician K-factors become greater in the 5G wideband channel system.

4.4. Spatial Parameters

4.4.1. RMS Angular Spread. On Line 1, the RMS angular spreads of angle of arrival (AoA) and angle of departure (AoD) are shown in Figure 7(a). ASA, ESA, ASD, and ESD are angular spreads of the azimuth angle of arrival, the elevation angle of arrival, the azimuth angle of departure, and the elevation angle of departure, respectively. The CDFs of angular spreads are illustrated in Figure 7(b).

In Figure 7, the ESA is relatively larger, and most (≥80%) values are greater than 10.7°, while the 80% of ASA are less than 7.8°, which explains there are more scatterers from the elevation domain at the Rx and the train body plays a major role. Then, the ESD is relatively smaller, and most (≥80%) values are less than 1.7° whereas the ASD is relatively larger and 80% are greater than 5.5°, which explains there are less scatterers at the elevation domain at the Tx. Besides, the measurement scenario in [28] is similar to the station scenario in the paper, and the results in [28] agree with the

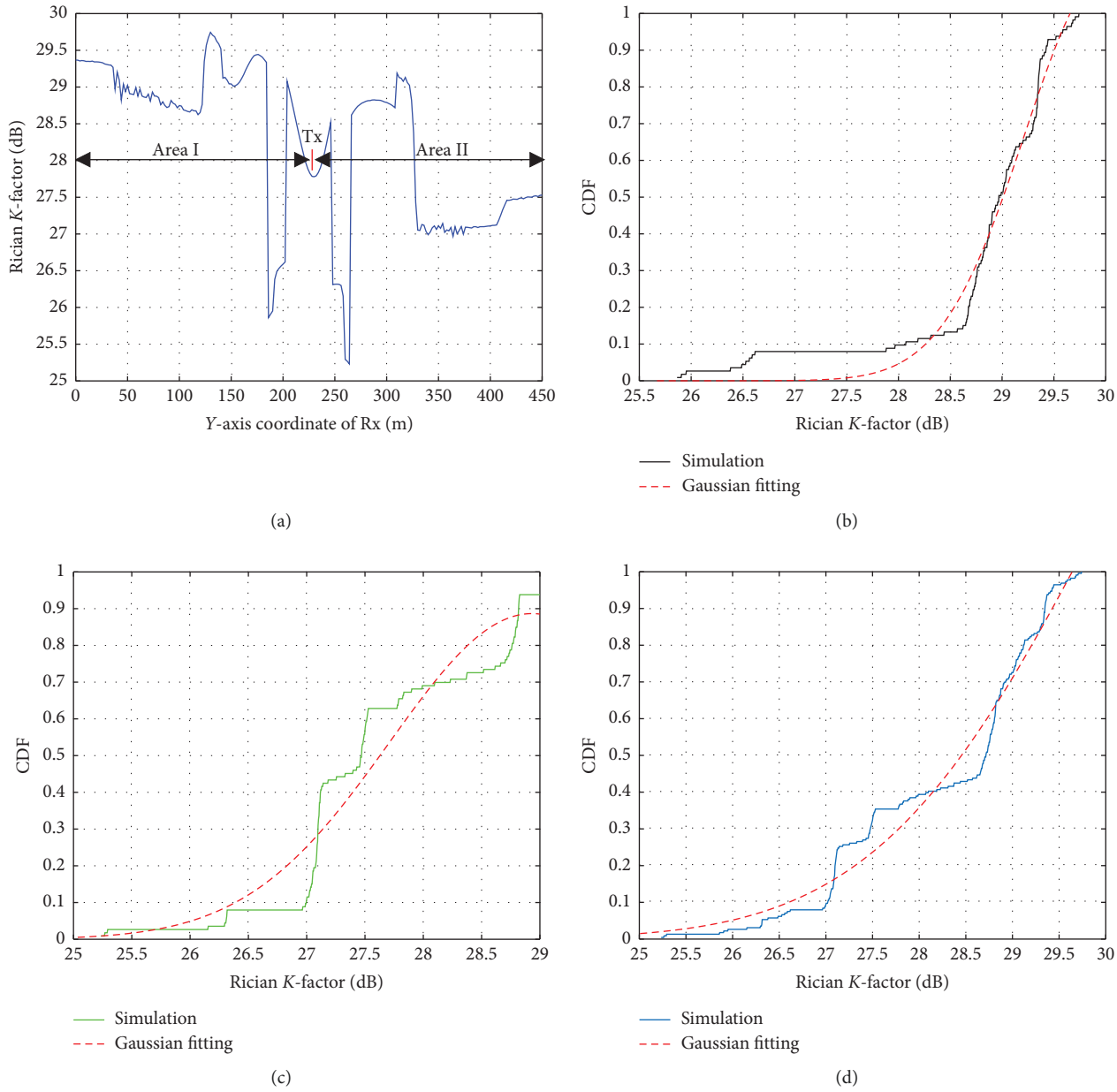

Figure 6: (a) Rician K-factor. (b) Area I. (c) Area II. (d) Line 1.

simulation results in the paper. Since there is a similar environment that more reflectors and scatterers in both scenarios, the scenarios have the same characteristic that the maximum of angular spread does not exceed 70°.

4.4.2. Power Angle Spectrum. In Figure 7(a), the angular spreads at two ends of the station are relatively small. That is why we need to focus on the power angle spectrum (PAS) [29] at two ends of the station. In this section, Figure 8 shows the PAS of AoA and AoD when the Y-axis coordinates of the Rx antenna are 6 m and 444 m, respectively.

In Figure 8(a), at the Y-axis coordinate 6 m, the main beam at Rx could be horizontal because values of normalized power are relatively the largest as the elevation angle of AoA is about 90°. Fortunately, elevation angle directions of the main beam are also distributed around 90° at the Y-axis coordinate 444 m. Furthermore, the relatively large ESA and horizontal beam at Rx show that the linear Rx antenna array should be perpendicular to the top of the train in order to achieve the low correlation among beams.

In Figure 8(b), at the 6 m, while the azimuth angle of AoD is about −20°, the normalized powers are the largest, which implies that the azimuth angle direction of the main beam at Tx could be about −20°. Conversely, at the 444 m, the azimuth angle directions of main beam are mainly distributed around 20°, but the elevation angles always approach 100°. Then, the ASDs of Tx antenna are greater than ESDs in Figure 7(a), which means the antenna array

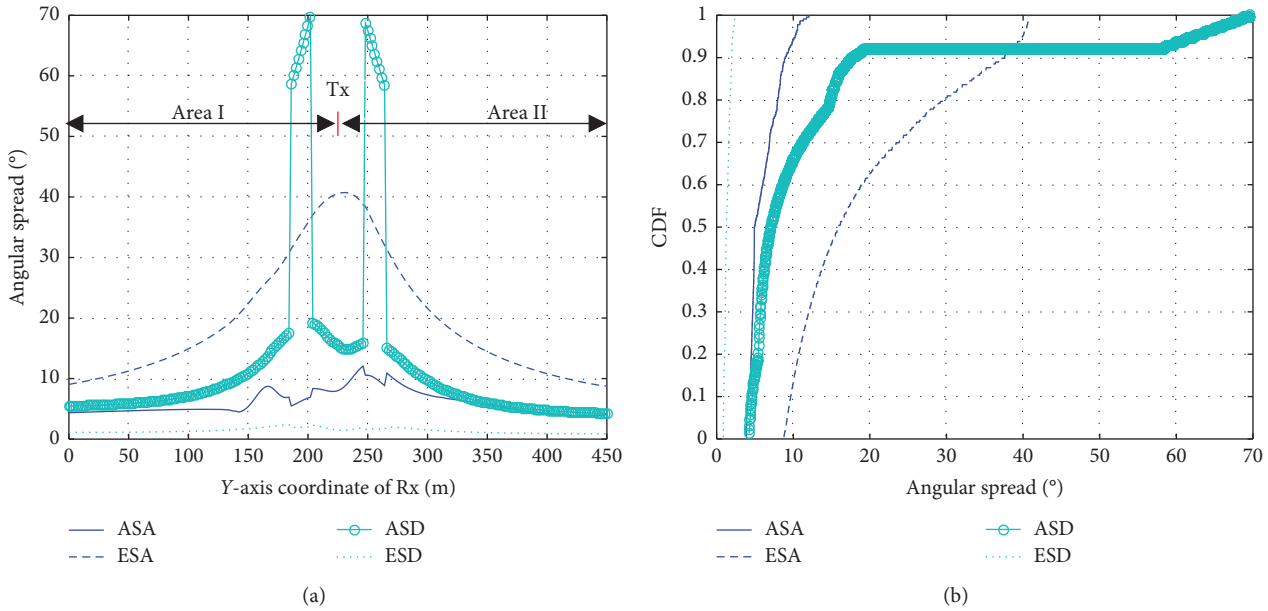

Figure 7: (a) RMS angular spread. (b) CDF of RMS angular spread on Line 1.

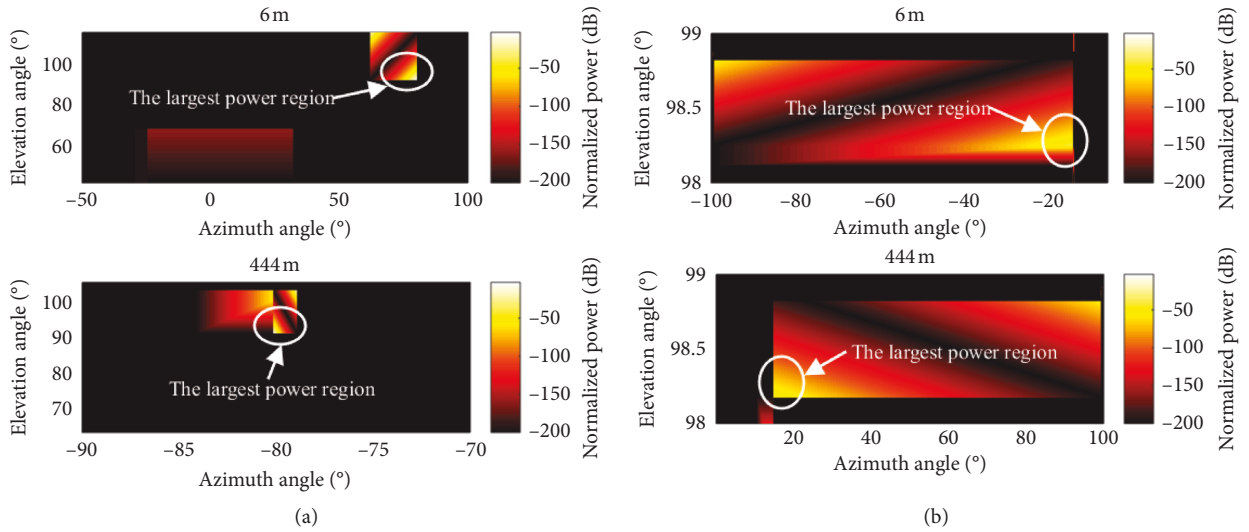

Figure 8: (a) PAS of AoA. (b) PAS of AoD.

could be horizontal and perpendicular to rails on the tower platform. Considering the direction of the main beam in Figure 8(b), the antenna array should be rotated counterclockwise or clockwise horizontally to be perpendicular to the direction of main beam for the low correlation.

4.5. Spatial Correlation. As we all know, the diversity gain and multiplexing gain of the MIMO system [30, 31] are directly related to the spatial characteristics of the channel. The above is the investigation of some spatial characteristic parameters at 5G mmWave band. In addition, as the important aspect of MIMO channels [32], the spatial correlation among beams must be discussed to achieve the suitable antenna spacing.

In this section, in order to improve the performance of the location where there is worser signal coverage, the angular spreads at that position are selected for correlation calculation to ensure the user experience of the overall scenario.

According to Figure 7(b), more than 90% of ASA and 90% of ESA are beyond 4.15° and 9.71°, respectively, and over 90% of ASD and 90% of ESD are larger than 4.64° and 0.92°, respectively, which result in the necessity of investigation about the spatial correlation among antenna elements in the case of relatively worser angular spread. The correlation coefficient between Rx antenna elements with ASA (4.15°) and ESA (9.71°) is shown in Figure 9(a), and the correlation coefficient of Tx antenna elements is drawn in Figure 9(b) as the ASD is 4.64° and ESD is 0.92°.

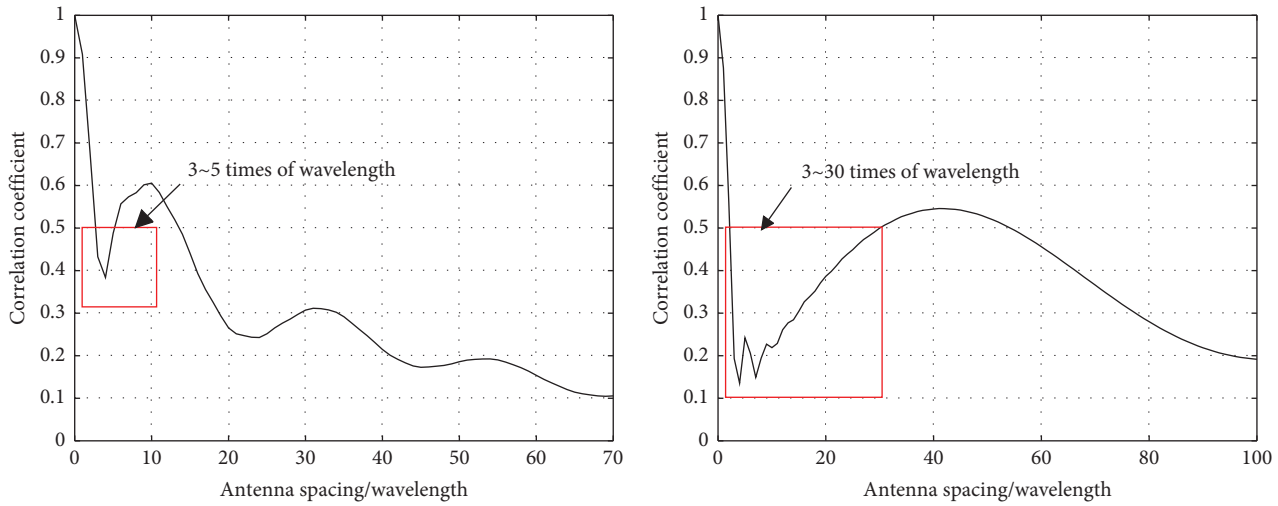

Figure 9: Correlation coefficient. (a) Rx antenna elements: ASA = 4.15°; ESA = 9.71°. (b) Tx antenna elements: ASD = 4.64°; ESD = 0.92°.

The wavelength at 40 GHz is approximately 7.5 mm. From Figure 9(a), the relative distance of Rx antenna array elements is at least 68 times to ensure that correlation coefficient between adjacent antenna elements is less than 0.1, but the antenna element spacing is around 51 cm that is too large to meet the engineering requirements. If the correlation coefficient can be relaxed to 0.5, it indicates the antenna element spacing only will be about 2.25~3.75 cm that might meet the requirement for application at the Rx.

In Figure 9(b), when the correlation coefficient of adjacent Tx antenna elements is less than 0.5, antenna spacing can be set to about 3~30 times of wavelength which means around 2.25~22.50 cm.

5. Conclusion

In this paper, channel characteristics of 5G mmWave band have been investigated at the high-speed railway station. Based on the measurement and simulation results, key channel parameters, such as path loss, delay spread, Rician K-factor, angular spread, PAS, and spatial correlation, are all analyzed. Some important results and suggestions are summarized as follows:

(1) When Tx antennas are installed on the tower, the maximum path loss on Line 1 is about 132.2 dB, which is so large that multiantenna technology is expected to ensure signal coverage strength and increase system capacity.

(2) The high-speed railway station is a semilimited space where the values of RMS delay spreads are almost less than 1.2 ns on Line 1, which is reasonable and acceptable in 5G systems.

(3) In the scenario, the Rician K-factors obey the Gaussian distribution which is owing to the large bandwidth in 5G systems.

(4) When the Tx and Rx both adopt uniform linear antenna arrays, the antenna spacing could be 2.25~22.50 cm at Tx, whereas the Rx antenna spacing might be set to 2.25~3.75 cm.

(5) The Rx antenna array should be vertical to the top of the train, while the horizontal Tx antenna array should be rotated counterclockwise or clockwise horizontally to obtain low correlation due to the propagation direction of the main beam.

(6) By analyzing the train's moving speed and the angle between the train's moving direction and incident wave direction, it can be found that the angle is approaching 90° as the Rx reaches the Tx, which makes Doppler shift decline. Due to simulation on Line 1 where the train needs to stop at the platform and the speed is relatively low, this paper does not focus on the Doppler effect and more related research could be conducted in future work.

Data Availability

The data used to support the findings of this study are available from the corresponding author upon request.

Conflicts of Interest

The authors declare that there are no conflicts of interest regarding the publication of this paper.

Acknowledgments

This work was supported by the National Key Research and Development Program under Grant 2016YFE0200900, NSFC under Grants 61725101 and U1834210, Beijing Natural Haidian Joint Fund under Grant L172020, Major Projects of Beijing Municipal Science and Technology Commission under Grant Z181100003218010, and the Royal Society Newton Advanced Fellowship (Grant no.: NA191006).

References

[1] T. S. Rappaport, Y. Xing, G. R. MacCartney, A. F. Molisch, E. Mellios, and J. Zhang, "Overview of millimeter wave communications for fifth-generation (5G) wireless networks—with a focus on propagation models," *IEEE Transactions on Antennas and Propagation*, vol. 65, no. 12, pp. 6213–6230, 2017.

[2] J. Zhang, Z. Zheng, Y. Zhang, J. Xi, X. Zhao, and G. Gui, "3D MIMO for 5G NR: several observations from 32 to massive 256 antennas based on channel measurement," *IEEE Communications Magazine*, vol. 56, no. 3, pp. 62–70, 2018.

[3] C. T. Neil, M. Shafi, P. J. Smith, P. A. Dmochowski, and J. Zhang, "Impact of microwave and mmWave channel models on 5G systems performance," *IEEE Transactions on Antennas and Propagation*, vol. 65, no. 12, pp. 6505–6520, 2017.

[4] D. He, B. Ai, K. Guan et al., "Channel measurement, simulation, and analysis for high-speed railway communications in 5G millimeter-wave band," *IEEE Transactions on Intelligent Transportation Systems*, vol. 19, no. 10, pp. 3144–3158, 2018.

[5] X. Cheng, L. Yang, and X. Shen, "D2D for intelligent transportation systems: a feasibility study," *IEEE Transactions on Intelligent Transportation Systems*, vol. 16, no. 4, pp. 1784–1793, 2015.

[6] B. Ai, X. Cheng, T. Kürner et al., "Challenges toward wireless communications for high-speed railway," *IEEE Transactions on Intelligent Transportation Systems*, vol. 15, no. 5, pp. 2143–2158, 2014.

[7] S. Priebe and T. Kürner, "Stochastic modeling of THz indoor radio channels," *IEEE Transactions on Wireless Communications*, vol. 12, no. 9, pp. 4445–4455, 2013.

[8] K. Guan, Z. Zhong, B. Ai, C. Briso-Rodriguez, and L. Zhang, "Large scale fading characteristics in rail traffic scenarios," in *Proceedings of the IEEE International Symposium on Antennas and Propagation & USNC/URSI National Radio Science Meeting*, pp. 83-84, Vancouver, Canada, July 2015.

[9] K. Guan, Z. Zhong, B. Ai, and T. Kürner, "Empirical models for extra propagation loss of train stations on high-speed railway," *IEEE Transactions on Antennas and Propagation*, vol. 62, no. 3, pp. 1395–1408, 2014.

[10] K. Guan, Z. Zhong, B. Ai, and T. Kürner, "Propagation measurements and analysis for train stations of high-speed railway at 930 MHz," *IEEE Transactions on Vehicular Technology*, vol. 63, no. 8, pp. 3499–3516, 2014.

[11] K. Guan, X. Lin, D. He et al., "Scenario modules and ray-tracing simulations of millimeter wave and terahertz channels for smart rail mobility," in *Proceedings of the 2017 11th European Conference on Antennas and Propagation (EUCAP)*, pp. 113–117, Paris, France, March 2017.

[12] L. Wang, K. Guan, B. Ai et al., "An accelerated algorithm for ray tracing simulation based on high-performance computation," in *Proceedings of the 2016 11th International Symposium on Antennas, Propagation and EM Theory (ISAPE)*, pp. 512–515, Guilin, China, October 2016.

[13] S. Priebe, S. Rey, and T. Kürner, "From broadband ray tracing propagation modeling to physical layer simulations of THz indoor communication systems," in *Proceedings of the IEEE Radio and Wireless Symposium*, pp. 142–144, Austin, TX, USA, January 2013.

[14] Y. Yoon, M. Jung, and J. Kim, "Intelligent ray tracing for the propagaiton prediction," in *Proceedings of the IEEE Antennas and Propagation Society International Symposium*, pp. 1-2, Chicago, IL, USA, July 2012.

[15] S. Sun, T. Rappaport, R. Heath, A. Nix, and S. Rangan, "MIMO for millimeter-wave wireless communications: beamforming, spatial multiplexing, or both?," *IEEE Communications Magazine*, vol. 52, no. 12, pp. 110–121, 2014.

[16] X. Cheng, Q. Yao, C.-X. Wang et al., "An improved parameter computation method for a MIMO V2V Rayleigh fading channel simulator under non-isotropic scattering environments," *IEEE Communications Letters*, vol. 17, no. 2, pp. 265–268, 2013.

[17] J. Zhang, Y. Zhang, Y. Yu, R. Xu, Q. Zheng, and P. Zhang, "3-D MIMO: how much does it meet our expectations observed from channel measurements?," *IEEE Journal on Selected Areas in Communications*, vol. 35, no. 8, pp. 1887–1903, 2017.

[18] L. Zhang, C. Briso, J. R. O. Fernandez et al., "Delay spread and electromagnetic reverberation in subway tunnels and stations," *IEEE Antennas and Wireless Propagation Letters*, vol. 15, no. 4, pp. 585–588, 2016.

[19] J. Zhang, C. Pan, F. Pei, G. Liu, and X. Cheng, "Three-dimensional fading channel models: a survey of elevation angle research," *IEEE Communications Magazine*, vol. 52, no. 6, pp. 218–226, 2014.

[20] G. R. MacCartney, T. S. Rappaport, and S. Rangan, "Rapid fading due to human blockage in pedestrian crowds at 5G millimeter-wave frequencies," in *Proceedings of the IEEE Global Communications Conference*, pp. 1–7, Singapore, December 2017.

[21] B. Yuan and H. Zhang, "Research on standard tower section in communication monopole," *Hans Journal of Civil Engineering*, vol. 7, no. 1, pp. 62–73, 2018.

[22] K. Guan, D. Zhong, B. Ai et al., "Deterministic propagation modeling for the realistic high-speed railway environment," in *Proceedings of the 2013 IEEE 77th Vehicular Technology Conference (VTC Spring)*, IEEE, Dresden, Germany, June 2013.

[23] D. He, B. Ai, K. Guan, L. Wang, Z. Zhong, and T. Kurner, "The design and applications of high-performance ray-tracing simulation platform for 5G and beyond wireless communications: a tutorial," *IEEE Communications Surveys & Tutorials*, vol. 21, no. 1, pp. 10–27, 2019.

[24] Y. Chen, F. Yang, and Y. Yu, "Research on 5G coverage capability," *Communications Technology*, vol. 51, no. 12, pp. 2866–2873, 2018.

[25] D. He, J. Yang, K. Guan et al., "Ray-tracing simulation and analysis of propagation for 3GPP high speed scenarios," in *Proceedings of the 2017 11th European Conference on Antennas and Propagation (EUCAP)*, pp. 2890–2894, Piscataway, NJ, USA, March 2017.

[26] "Study on channel model for frequency spectrum above 6 GHz (Release 15)," 3rd Generation Partnership Project (3GPP) TR 38.900-15.0.0, June 2018.

[27] Z. Wang, P. Wang, and H. Xiong, "Estimation and measurement of K parameter for rice fading channel," *Journal of Data Acquisition & Processing*, vol. 24, no. 1, pp. 109–113, 2009.

[28] S. Hur, J. H. Park, T. Kim et al., "Wideband spatial channel model in an urban cellular environments at 28 GHz," in *Proceedings of the European Conference on Antennas & Propagation*, Lisbon, Portugal, April 2015.

[29] W. Meng, D. Wei, and S. Gong, "Power angle spectrum of satellite communication downlink in rainfall environment," in *Proceedings of the IEEE International Symposium on Microwave*, pp. 373–377, Chengdu, China, October 2013.

[30] N. Khalid and O. B. Akan, "Experimental throughput analysis of low-THz MIMO communication channel in 5G wireless

networks," *IEEE Wireless Communications Letters*, vol. 5, no. 6, pp. 616–619, 2016.

[31] A. A. Kalachikov and N. S. Shelkunov, "Performance evaluation of the detection algorithms for MIMO spatial multiplexing based on analytical wireless MIMO channel models," in *2018 XIV International Scientific-Technical Conference on Actual Problems of Electronics Instrument Engineering (APEIE)*, pp. 180–183, Novosibirsk, Russia, October 2018.

[32] U. Karabulut, A. Awada, I. Viering, M. Simsek, and G. P. Fettweis, "Spatial and temporal channel characteristics of 5G 3D channel model with beamforming for user mobility investigations," *IEEE Communications Magazine*, vol. 56, no. 12, pp. 38–45, 2018.